

Real-Time Optical Flux Limits From Gamma-Ray Bursts

Measured By

The GROCSE Experiment

H. S. Park¹, E. Ables¹, D. L. Band⁵, S. D. Barthelmy^{3,7}, R. M. Bionta¹, P. S. Butterworth³,
T. L. Cline³, D. H. Ferguson⁶, G. J. Fishman⁴, N. Gehrels³, K. Hurley⁸, C. Kouveliotou⁴,
B. C. Lee², C. A. Meegan⁴, L. L. Ott¹ and E. L. Parker¹

Received _____; accepted _____

¹Lawrence Livermore National Laboratory, Livermore, CA 94550

²Dept. of Physics, University of Michigan, Ann Arbor, MI 48109

³NASA/Goddard Space Flight Center, Greenbelt, MD 20771

⁴NASA/Marshall Space Flight Center, Huntsville, AL 35812

⁵CASS 0424, University of California, San Diego, La Jolla, CA 92093

⁶Dept. of Physics, California State University at Hayward, Hayward, CA 94542

⁷Universities Space Research Association

⁸Space Sciences Laboratory, University of California, Berkeley, CA 94720-7450

ABSTRACT

The Gamma-Ray Optical Counterpart Search Experiment (GROCSE) presents new experimental upper limits on the optical flux from gamma-ray bursts (GRBs). Our experiment consisted of a fully-automated very wide-field opto-electronic detection system that imaged locations of GRBs within a few seconds of receiving trigger signals provided by BATSE's real-time burst coordinate distribution network (BACODINE). The experiment acquired 3800 observing hours, recording 22 gamma-ray burst triggers within ~ 30 s of the start of the burst event. Some of these bursts were imaged while gamma-ray radiation was being detected by BATSE. We identified no optical counterparts associated with gamma-ray bursts amongst these events at the $m_V \sim 7.0$ to 8.5 sensitivity level. We find the ratio of the upper limit to the V-band optical flux, F_ν , to the gamma-ray fluence, Φ_γ , from these data to be $2 \times 10^{-18} < F_\nu/\Phi_\gamma < 2 \times 10^{-16}$.

Subject headings: gamma rays: bursts

1. Introduction

Cosmic GRBs are arguably the most intriguing phenomena in modern high energy astrophysics. Resolving the mystery of the origin of gamma-ray bursts will probably require the discovery of counterpart radiation in other wavebands, particularly in the optical band. Detailed study of such a counterpart might reveal the physical mechanisms of the GRB process while even a single unambiguous distance measurement could determine the burst distance scale. At the very least, upper limits at other frequencies constrain sources' multi-wavelength characteristics and thus possible emission mechanisms. Given the possibility that GRBs may represent hitherto unexplored physical regimes, it is not surprising that several of near simultaneous counterpart searches are in progress (see Hudec 1995a, b and references therein). Here we report on the results of two years of operation of the Gamma-Ray Optical Counterpart Search Experiment (GROCSE).

Counterpart emission can be described as flaring, fading, or quiescent (Schaefer 1994). Flaring emission would be simultaneous with the burst observed in the gamma-ray band. One approach to observing the flaring emission is to scan the sky independent of the gamma-ray detector. This is the strategy of the Ondrejov photographic network (Hudec 1993; Greiner et al. 1992, 1994, and 1995; Hudec et al. 1995b), and the Explosive Transient Camera (ETC–Vanderspek et al. 1994). It was also the intended strategy of the ill-fated High Energy Transient Explorer (HETE–Ricker et al. 1988). Alternatively, a detector can respond rapidly to a burst trigger from a gamma-ray instrument, catching a burst in its later phase. This approach was used by GROCSE and has been adopted by other operational systems as well: the BATSE-COMPTTEL-NMSU network (McNamara 1996), the Livermore Optical Transient Imaging System (LOTIS) (Park 1997), and the Department of Defense GEODSS system. Burst coordinates are currently distributed in near real-time by the BATSE CO-ordinate DIstribution NETwork (BACODINE–Barthelmy et al. 1994), which

monitors BATSE data on board and responds to bursts by calculating and distributing preliminary burst positions.

Optical emission may come from the burst source or its environment after the gamma-ray emission ends. Such emission, if luminous enough, would allow detection of a source not previously present in the seconds-to-days after a GRB and which would subsequently fade. There are currently a large number of optical and radio experiments, including those searching for flaring emission mentioned above. These search experiments may be characterized by the energy band searched, the depth of the search (e.g. the limiting magnitude), and the time between the burst and the search (McNamara 1995). The depth-of-search improves as the GRB-to-optical observation time interval increases due to lag times necessary to compute minimum-field error boxes and to arrange observations on large telescopes. For example, the typical limiting magnitude on time scales of hours is $m_V \sim 8$, while it improves to $m_V \sim 22$ on time scales longer than 1 day. Most of these searches for fading emission use BACODINE positions. If a burst location also happens to fall within the COMPTEL or EGRET fields-of-view, a more precise position can be distributed in a matter of days. On similar time scales, the Interplanetary Network, which currently consists of only one long baseline (Earth-Ulysses–Hurley et al. 1994, 1997), provides arcs only a few arcseconds wide.

The smaller error boxes obtained at longer time scales have been searched by a variety of powerful telescopes in different wavebands. Objects potentially of interest will be found if a small region of the sky is searched sufficiently deep, and therefore the issue is whether any likely sources are found. Such searches might detect an interesting object within the error boxes if bursts originate within the Galaxy. If bursts instead originate at extragalactic distances, then a galaxy is expected in the error box. In particular, a bright burst is presumably relatively nearby and its host galaxy should be bright. Bright bursts

can usually be localized to smaller error boxes, diminishing the probability of an unrelated bright galaxy in the error box.

There are no firm predictions of expected optical emission because the origin and nature of GRBs are uncertain. Schaefer’s report of optical transients on archival photographic plates (Schaefer 1981; Schaefer et al. 1984) led to a number of theoretical models that in general attempted to explain the apparent magnitudes of these optical transients. These theories included reprocessing gamma rays in a stellar companion’s atmosphere (London & Cominsky 1983; London 1984; Rappaport & Joss 1985; Melia, Rappaport, & Joss 1986; Cominsky, London, & Klein 1987) or in an accretion disk (Epstein 1985; Melia 1988). Other theories attributed optical-ultraviolet emission to processes in a neutron star magnetosphere (Liang 1985; Katz 1985; Bisnovatyi-Kogan & Illarionov 1986; Sturrock 1986; Ruderman 1987; Hartmann, Woosley, & Arons 1988; Hameury & Lasota 1989; Ho & Epstein 1989, Dermer 1990) and assumed source distances of order 100 pc. The latter theories were largely invalidated by the BATSE observations, which placed large lower distance limits and instead support Galactic halo or cosmological models. Ford & Band (1996) found by simple extrapolation of burst spectra that, at any given site, flaring emission would be observable from only a few bursts per year with $m_V \sim 10$ to 15. The brighter predicted optical fluxes result from bursts with soft gamma-ray spectra. If we instead assume the low energy photon spectrum is $F_\gamma \propto E^{1/3}$, as expected for synchrotron emission from an electron distribution with a low-energy cutoff (Katz 1994; Tavani 1996a, b), then the predicted distribution of optical fluxes will be shifted towards fainter magnitudes.

A number of theories suggest that fading optical emission may be observable as a result of reprocessing of burst radiation by the medium surrounding the burst source: Jennings (1983) considered $H\alpha$ line radiation from resonant scattering and recombination, while Chevalier (1986), Schaefer (1987), and Katz & Jackson (1988) investigated dust scattering

of radiation from an optical transient. These models predict that ionizing radiation is reprocessed to optical radiation in a manner thus far unobserved. The fading emission is proportional to the burst fluence and the density of the reprocessing region. For sufficiently large optical emission, the density must be $n \sim 10^5 \text{ cm}^{-3}$ (Band & Hartmann 1992). These models were constructed within the paradigm of local burst sources and thus do not provide usable optical predictions, if one accepts the current paradigm of halo cosmological distances.

In cosmological fireball models, a relativistically expanding fireball radiates at the shocks formed either as the ejecta within the fireball impact the surrounding medium (Rees & Meszaros 1992; Meszaros & Rees 1993; Meszaros, Rees, & Papathanssiou 1994; Katz 1994; Sari, Narayan, & Piran 1996) or as a consequence of inhomogeneities within the expanding fireball (Rees & Meszaros 1994; Paczynski & Xu 1994; Papathanssiou & Meszaros 1996). In these models, the spectrum extends from the gamma ray to the optical band during the burst itself (e.g. Papathanssiou & Meszaros 1996). In addition, the optical emission may last for hours after the end of the gamma ray emission. The predicted optical flux and its temporal evolution are highly model-dependent. For example, in considering fading optical emission for a variety of models, Meszaros & Rees (1997) find $9 \leq m_V \leq 19$ which fades as $A \log t(s)$ where $3.75 \leq A \leq 15$. These cosmological models will thus undoubtedly accommodate upper limits and possible detection from GROCSE and successor experiments.

The BATSE gamma-ray detectors provide burst positions localized only within wide angular limits, $1 \sim 10^\circ$, depending on burst brightness and duration (Meegan 1996). A system that seeks to detect an optical counterpart near-simultaneously with the GRB must be on-location within a few seconds and image over a field-of-view roughly 15° across. GROCSE was the first operational instrument satisfying these criteria. GROCSE collected

images of burst error boxes shortly after the bulk of the gamma-ray emission, and therefore the GROCSE results place the strongest constraints yet on optical counterparts of fading GRB emission on time scales of tens of seconds from the GRB peak.

2. GROCSE Instrumentation

The basic requirements to search for GRB optical counterparts are: receiving and processing in near-real time GRB coordinates; a $> 15^\circ$ field of view telescope system to cover the large angular uncertainty of the BATSE gamma-ray detectors onboard the Compton Gamma-Ray Observatory; and a rapidly-slewing telescope mount capable of slewing to the GRB field within a few seconds. GROCSE received near-real time GRB coordinates from BACODINE which uses real-time data from the satellite, computes burst coordinates using the weighted triangulation method, and transmits the information via the Internet (Barthelmy 1994). The "internal socket" protocol we employed for data communication between NASA/Goddard Space Flight Center (GSFC) and our observation site at the Lawrence Livermore National Laboratory (LLNL) established special dedicated links to transmit and receive pre-formatted data packets. We verified the connection once per minute during observations by sending test packets. The link has transmitted data reliably for over 3 years. The average delay from the BATSE trigger to receipt by the GROCSE pointing and control software is ~ 5.5 s. Our electro-optical sensor and data recording equipment derived from a system originally constructed for a low-Earth orbit satellite tracking program (Park 1990). It featured a very large, fast-slewing alt-azimuth telescope mount and unique wide-field optics. The hardware is shown and illustrated schematically in Figure 1. A fish-eye lens constructed of solid blocks of concentric spherical elements produces uniform spot sizes across the entire lens field of view of 60° . The effective aperture of this lens is 89 mm and the focal length is 250 mm. We covered the large spherical focal

area ($> 500 \text{ cm}^2$) with 23 segments of custom fiber optic reducers (3.8:1 reduction ratio). The front of each fiber bundle was machined to match the curvature of the spherical lens for best focus. Each focal reducer mapped an $8 \times 11^\circ$ field of view onto an $8\text{mm} \times 13\text{mm}$ flat CCD area.

The schematic of the data acquisition system is shown in Figure 2. The 23 cameras were clocked synchronously by a master clock and timing distribution box. The gain of each intensifier was computer controlled through a CAMAC interface. The exposure duration for all GROCSE images was set by the length of the intensifier gate pulse to 0.5 s. The entire lens and camera assembly was mounted on a Contraves, Goertz, Inc. computer-controlled inertial guidance indexing table. The mount provided a maximum angular slew rate of 1000/sec with pointing precise to ~ 1 arcsec. Our data collection system was hosted by a SUN 4/330 computer. The camera output was directed to an 8 bit digitizer by means of a 23 channel video multiplexer. Following digitization, these data were collected and formatted by a Datacube image processing system, time-tagged using a WWVB clock, and then stored on disk. In addition, all GRB events were archived to Exabyte tape. The Sun 4/330 host also provided pointing commands to the Contraves, Goertz, Inc. mount via a GPIB interface. In addition, the computer performed various housekeeping controls, such as monitoring the precipitation detector for indications of rain or fog and closing a weathertight clam shell over the instrument during periods of daylight or inclement weather. The on-line software automatically activated the instrument shortly after sunset and reestablished the connection to BACODINE. While awaiting GRB triggers, GROCSE collected data across the entire sky every 30 minutes, recording suitable sky background data for analysis of any GRB events across the entire unobstructed sky. We limited our observations to more than 30° above the horizon because buildings surrounding the system, which was necessarily on-site at LLNL, blocked the view at lower angles. This "sky patrol" was interrupted whenever BACODINE sent GRB coordinates. If such a coordinate set was

within the field of regard of the telescope system and not within 30° of the Moon, GROCSE was slewed at rapid rate to the location of the GRB candidate and images were recorded for 20 minutes after the trigger. GROCSE then returned to "sky patrol" mode until either another GRB occurred or dawn broke. The software was programmed to deactivate the camera and close the clam shell before dawn. GROCSE operated between 1994 January and 1996 June for 3,800 hours (Lee 1997). The instrument operated approximately 52% of available night-hours. GROCSE recorded 22 burst triggers during the period of operation.

3. GROCSE Gamma-Ray Burst Observations

The basic analysis strategy was to search the resulting images of GRB location for "new" star-like objects that do not appear in the star catalogues or in the background sky patrol images. The task of identifying stars in the imagery was complicated by the noisy intensifier data, the necessity to reject ion events, and differences in field distortion between all detectors due to variations in the microchannel plate bundle uniformities. We utilized a program that automatically matched known positions of bright stars to stellar locations from GROCSE images. Ambiguity occasionally existed, such as in field areas suffering from high microchannel plate distortion, in crowded fields, or where an cosmic ray event may have occurred. In these cases the operator examined carefully the star image in question to either assign a bright star, or if the datum in question subtended only one pixel, reject the point as an cosmic ray event. We found the method to be very reliable except for double stars with known separations between $50''$ and $300''$, in which case very careful comparison of stellar coordinates with image pattern was required. All images from 13 GRB triggers was examined in this fashion. None of the images contained any evidence for "new" star like objects.

We derived upper limits to in-band fluxes of gamma-ray bursts shortly after outburst

peaks by computing the sensitivity of GROCSE from observations of stars obtained in the GRB field. This process circumvented the need to radiometrically calibrate the individual sensors each night. Our data yield a completeness limit across observed gamma-ray burst events of $m_{V,complete} \sim 6.75 \pm 0.25$ 1- σ , which corresponds to a flux density $F_\nu(5500\text{\AA}) = 7.5 \pm 0.7 \times 10^{-23}$ ergs-cm⁻²-s⁻¹-Hz⁻¹. Our limiting magnitude is $m_{V,limit} \sim 7.4 \pm 0.4$ 1- σ , or a respective flux density $F_\nu(5500\text{\AA}) = 4.1 \pm 0.8 \times 10^{-23}$ ergs-cm⁻²-s⁻¹-Hz⁻¹. Note that the completeness magnitude is defined as the level for which all stars are observed while the limiting magnitude is the brightness where only half the stars are observed.

The GROCSE GRB data are summarized in the first seven columns of Table 1. Column 1 lists the GRB name from their recorded UTC date. The BATSE trigger number is listed in column 2. We analyzed 13 of the 22 total GRBs. The other events were rejected due to cloud conditions or a error in BACODINE position. Our measured limiting visual magnitude m_V is shown in column 3, then converted to frequency-dependent flux at 5500 \AA $F_\nu(5500\text{\AA})$ as listed in column 4. Column 5 shows the time delay td from the beginning of the burst to the collection time of the optical images and column 6 specifies the gamma-ray burst duration time (T_{90}) measured by BATSE. Columns 5 and 6 can be compared to see if a given GRB was imaged optically while the gamma-ray event was still in progress. Column 7 gives the percent of the BATSE 3- σ error box imaged by GROCSE.

We have selected three BATSE triggers, GRB951117, 951124, & 951220 from our observations to show some of the event characteristics and analysis. The IPN annuli are available for these events which give smaller positional error. Figure 3-5 shows BATSE light curves for the three events and the BATSE 3- σ error circle for the three events in question, each superimposed on the GROCSE rectangular field. A systematic error of 1.6 $^\circ$ is included. Burst number, date, limiting magnitude, and the fraction of the BATSE error circle superscribed by the GROCSE frame are given for each event.

We considered the effect of the uncertainties in stellar effective temperatures, variable stars, differences between cameras in our focal plane array, sky background, and star identification errors. Stars with a range of effective temperatures were observed across the approximately 0.32-0.70 μm in-band sensitivity region of the S-20 photocathodes. Stars of different spectral types, when combined with the wavelength-dependent instrument response function, will have varying ratios, Δm_{VT} , of apparent m_V at 5550 \AA to in-band flux. This quantity was computed for a variety of effective temperatures where

$$\Delta m_{VT} = -2.5 \times \log \left(\frac{\int_{\lambda_b}^{\lambda_r} B_\lambda(T) \tau_{inst} \tau_{atm} \eta d\lambda / B_{5500\text{\AA}}^\circ(T, \theta)}{\int_{\lambda_b}^{\lambda_r} B_\lambda(10,000\text{K}) \tau_{inst} \tau_{atm} \eta d\lambda / B_{5500\text{\AA}}^\circ(10,000\text{K}, \theta)} \right). \quad (1)$$

Here, θ is the zenith angle, $B_\lambda(T)$ is the blackbody flux at wavelength λ for stellar effective temperature T , τ_{inst} is the wavelength-dependent instrument throughput to the sensor, τ_{atm} is the wavelength and zenith angle-dependent atmospheric transmission (Allen 1976), and η is the S-20 photocathode quantum efficiency. Given, as we shall see, that the magnitude spread in our observations is considerably larger than the color effect component, we approximated stellar energy distributions with Planck distribution for ease of calculation. These differences amounted to no more than $\Delta m_{VT} = \pm 0.13$, $1-\sigma$, for stars with effective temperatures ranging from 3000 K to 20,000 K with a distribution of equal numbers of stars per unit linear temperature. This is clearly a very conservative upper limit to temperature sensitivity because the vast majority of all stars observed to a limiting magnitude $m_V < 7.5$ have effective temperatures between 4,000 K and 15,000 K. The dependence of Δm_{VT} on zenith angle is small compared with the effect of the rapidly changing S-20 photon response with wavelength.

There are of order 10^4 variable stars listed in Kholopov (1987) distributed across $\sim 10^4$ square degrees of sky, or of order one variable star per square degree. Including as it does all known variable stars, the Kholopov sample is increasingly complete for stars of brighter apparent magnitude and wider brightness variation. We are interested in stars of $m_V \leq 8$

and effects on star counts of $\Delta m_V > \pm 0.1$. At this relatively bright limiting magnitude and amplitude range, the sample is essentially complete and still accounts for well less than one star per camera frame. Hence, the effect of variable stars biasing our sample is negligible compared with the star match error in m_V .

Throughput differences between the cameras, due largely to varying sensitivities of the S-20 photocathodes, amount to $\Delta m_{V\text{cathode}} \sim 0.2$. This effect is significant but smaller than the star match magnitude error due to the predominance of the sky background.

We estimate our best-case scattered light level at about $m_V = 8.0$. Our resolution element angular size is 72 arcsec square, which corresponds to a background level of $m_V = 10.2$ per pixel for the best local limiting magnitude of 19.5 per square arcsecond. Unfortunately, the instrument was located near bright outdoor lighting, which increased the background by a factor of several due to scattering by local dust and aerosols. Events occurred at various angular distances from the Moon and at a variety of lunar phases, significantly increasing the background for certain events. The data show that both the limiting magnitude and the completeness of star matches varied between gamma-ray bursts by $\Delta m_V \sim 0.5$. Similar results are expected for sky background-limited data.

In summary, $\Delta m_{V\text{complete}} \cong m_{V\text{limit}} \cong 0.5$ over all events is consistent with the sky background variations dominating our flux uncertainty values, albeit with instrumental noise and a slight star temperature uncertainty contribution as well.

4. Connection Between Optical Limits and Gamma-ray Observations - Discussion and Summary

We want to relate the observed optical energy flux $F_\nu(\nu_o)$, (units of $\text{ergs-cm}^{-2}\text{-s}^{-1}\text{-Hz}^{-1}$) at a fiducial frequency ν_o to the gamma-ray observations of the burst. For each burst,

we have a series of optical upper limits from images taken between t_b and t_e . Clearly an optical upper limit is more constraining for a bright GRB than for a weak one. The comparisons between the two energy bands are model-dependent since the choice of optical and gamma-ray quantities which are compared must be based explicitly or implicitly on an assumed physical connection between these quantities. In general, we have limits on the optical emission after the gamma-ray emission ends, while only in a few cases do we have limits on the optical emission during the burst. Nor can we say much about the bolometric optical emission because we do not know what spectral shape we are constraining. The comparisons between gamma-ray and optical quantities are not unique; in particular, they can be scaled by constant factors such as fiducial energies and frequencies. Ultimately we present quantities which can be used to constrain detailed physical models. Our data support three different methods of comparing the optical and gamma-ray observations.

Suppose first that optical emission is produced in the same region as the gamma rays by related physical mechanisms. The optical flux then scales with the gamma-ray photon flux at a fiducial energy E_γ , for example if the optical spectrum is an extrapolation of the gamma-ray spectrum (Ford & Band 1996). For an event captured optically while the GRB was still in progress, the optical $F_\nu(\nu_o)$ should be compared to the gamma-ray energy flux $F_\gamma(E_\gamma)$ (ergs-cm⁻²-s⁻¹-keV⁻¹) at E_γ (keV) averaged over the same time period as the image corresponding to F_ν . This comparison suggests a simple ratio

$$R_1 = 2.42 \times 10^{17} \frac{\text{Hz}}{\text{keV}} \frac{F_\nu}{F_\gamma(E_\gamma)} \quad (2)$$

or an effective energy spectral index

$$\alpha_{0\gamma} = \frac{\log\left(2.42 \times 10^{17} \frac{\text{Hz}}{\text{keV}} F_\nu / F_\gamma(E_\gamma)\right)}{\log(E_\gamma / h\nu_o)} \quad (3)$$

where E_γ and $h\nu_o$ must be expressed in the same units.

In the second case, optical emission may result from immediate reprocessing of

the gamma-ray flux. Then the optical flux at any moment during the burst would be proportional to the gamma-ray energy flux ($\text{ergs-cm}^{-2}\text{-s}^{-1}$). If an optical image was accumulated from t_b to $t_e = t_b + \Delta t$, F_ν should be compared to

$$\Phi_\gamma = \frac{1}{\Delta t} \int_{t_b}^{t_e} dt \int dE F_\gamma(E, t) \quad (4)$$

where the integration proceeds over the model-dependent gamma-ray energy range. A useful dimensionless quantity is

$$R_2 = \frac{F_\nu \nu_o}{\Phi_\gamma} \quad . \quad (5)$$

In this expression, ν_o converts the optical energy flux per unit frequency into a broadband energy flux. This quantity is approximately the inverse of the Schaefer (1981) L_γ / L_{opt} integrated over the B-band.

Optical emission in a third case might be proportional to GRB fluence following a time delay. The most important strength measure would be the total GRB energy released, which is proportional to the burst fluence ϕ_γ observed at Earth. Thus the optical flux limits F_ν after the burst should be compared with ϕ_γ . The ratio

$$R_3 = \frac{F_\nu}{\phi_\gamma} \quad (6)$$

is dimensionless (the units of F_ν , $\text{ergs-cm}^{-2}\text{-s}^{-1}\text{-Hz}^{-1}$ include the dimensionless factor $\text{s}^{-1}\text{-Hz}^{-1}$). Note that optical R_3 could be multiplied by $\nu_o \Delta t$ and still remain dimensionless. Multiplying F_ν by $\nu_o \Delta t$ would convert the energy flux per unit frequency into a fluence; formally, this latter form of R_3 compares similar optical and gamma-ray quantities. We are instead interested in describing the optical response at a given time to a burst of a specified intensity so the characterization of the response a time after the burst should be independent of the time over which an image is integrated. We thus prefer to leave out this factor of $\nu_o \Delta t$ from the definition of R_3 .

GROCSE often did not view the error box until the burst was over. The comparison

in such circumstances is best made between the optical upper limit and the gamma-ray fluence, or R_3 (eq. 6). For those bursts where the optical observation occurred while the burst was still in-progress, the gamma-ray fluence up to the time of the optical observation should be used, although in actuality both cases of a GROCSE observation occurring during a GRB caught only the trailing edge of the burst after almost all the GRB energy emission.

Adequate data is made available to accommodate calculation of such model-dependent temporal variations. Gamma-ray fluences can be derived from several types of BATSE data products. We have the highest confidence in fluences calculated by integrating the burst photon spectrum over energy and time when the spectrum is fit to the SHERB datatype, which provides sufficient spectral and temporal resolution. The SHERB data are a series of count spectra accumulated by the BATSE Spectroscopy Detectors (SDs); except for the longest bursts (none of which were observed by GROCSE), there are SHERB spectra after the end of each burst which help in extrapolating the background spectrum during the burst.

When there are no SHERB spectra for one reason or another (e.g., the SHERB spectra are not returned in the telemetry for weak bursts, or data are lost in telemetry gaps or gaps in collection), we used the fluences from the 3B catalog (Meegan et al. 1996), when available. These fluences are provided over the 20-2000 keV range. Finally, we used fluences derived from fits to the STTE spectra which are also from the SDs. The STTE data are the arrival times and energies of 64,000 counts around the time of the burst trigger from various detector modules; these counts can be accumulated over a variety of time scales. The STTE data do not necessarily span the entire burst duration nor do they provide sufficient background data to assist in interpolating its background spectra at the time of the burst. Thus we use the STTE data as a last resort.

The results of this comparison are presented in columns 8 through 10 of Table 1.

Column 8 describes the gamma-ray fluence ϕ_γ in units of ergs-cm^{-2} over the energy range 20-2000 keV. The ratio of optical flux to gamma-ray fluence R_3 , the ratio of the optical flux upper limit to the gamma-ray fluence is shown in column 9. Note that this ratio is an upper limit. Column 10 provides notes as applicable to each burst. Table 2 shows values of Φ , R_1 , and R_2 for selected GRBs, as defined in equations (4), (2), and (5), respectively for simultaneous optical gamma-ray emission. Note that the upper limits are given for the latter two quantities.

If the optical limit was set during the gamma-ray burst, upper limits for in-band gamma-ray flux can be computed based on extrapolating eq. (2) to visible wavelengths. Burst spectra can be fitted with the "GRB" spectral function (Band et al. 1993). Here, the gamma-ray energy spectra are modeled in terms of two components: a high-energy component and a low-energy component of functional form

$$N(E) = \frac{F_\gamma}{E_\gamma} = AE^\alpha e^{-E/E_o}, \quad E \leq (\alpha - \beta)E_o \quad (7a)$$

for low energies and

$$N(E) = BE^\beta, \quad E > (\alpha - \beta)E_o \quad (7b)$$

for high energies, where the parameters A, α , B, and β vary amongst gamma-ray bursts, and $\alpha > \beta$. The energy breakpoint is chosen so that $N(E)$ and its derivative are continuous at E_o , typically 100 keV to >1 MeV.

Fortuitously, several bursts appeared to be in progress at the moment of GROCSE imaging, among them GRB 951220 and 951124. There are no SHERB data for GRB 951220 and the STTE data are inadequate to determine the gamma-ray flux during the optical observation. Thus, an energy flux from GRB 951220 may be computed from observations although insufficient data exist to reconstruct a spectrum. The GRB 951124 optical observation occurred on the falling edge of the first of two gamma-ray flux peaks. Based on the evolution of the spectrum as gleaned from SHERB data, 90% of the energy flux resides

in the first peak. Flux results up to the optical observation and for the entire event are presented in Table 1. The GROCSE observation began 30 s after the BACODINE trigger. The SHERB data were accumulated at the following post-trigger times: 26.75, 28.8, 31.30, & 34.30 s. Due to the small number of counts and variable count rate, as expected from a highly dynamic spectral evolution, determination of the instantaneous spectrum at $t = 30.0$ s is somewhat imprecise. The best fit is:

$$N(E) = 8.413 \times 10^{-3} \left(\frac{E}{100 \text{ keV}} \right)^{-0.3464} e^{-E/85.9} \quad , \quad E \leq 177.75 \text{ keV}, \quad (8a)$$

$$N(E) = 3.493 \times 10^{-3} \left(\frac{E}{100 \text{ keV}} \right)^{-2.416} \quad , \quad E > 177.75 \text{ keV}. \quad (8b)$$

In conclusion GROCSE did not observe optical counterparts to GRBs to levels described in Table 2. Proper physical mechanisms for GRBs must not yield optical components larger than these new upper limits.

GROCSE was decommissioned in June, 1996 following two years of successful operation, in order to concentrate on the next-generation instrument LOTIS, a fast-slewing wide-field lens array featuring four Loral 2048×2048 CCDs capable of searching to below $m_V = 14$. LOTIS is now fully-operational and results from this new experiment will be presented in a forthcoming paper.

This work was supported by the U.S. Department of Energy, under contract W-7405-ENG-48 to the Lawrence Livermore National Laboratory and NASA contract S-57771-F. Gamma-ray burst research at UCSD (D. Band) is supported by NASA contract NAS8-36081. K. Hurley acknowledges JPL Contract 958056 for Ulysses operations and NASA Grant NAG5-1560 for IPN work. Brian Lee is grateful for the support of his work by grant NGT-52805 under the NASA Graduate Student Researchers Program. We also acknowledge C. Akerlof from Univ. of Michigan for his participation of this experiment.

Table 1. Summary of GROCSE Event Characteristics.

Name	BATSE Trigger	m_V V	$F_\nu(5500\text{\AA})^a$	t_d^b s	T_{90}^c s	Cov^d %	F_γ^e	R_3	notes
940129	2793	7.3	4.58×10^{-23}	35	7	75	1.53×10^{-5}	2.94×10^{-18}	f,k
940623	3040	7.3	4.58×10^{-23}	17.4	26	80	2.88×10^{-6}	1.56×10^{-17}	g
		7.3	4.58×10^{-23}	20.3			3.10×10^{-6}	1.45×10^{-17}	g
		7.3	4.58×10^{-23}	24.1			3.28×10^{-6}	1.37×10^{-17}	g
		7.3	4.58×10^{-23}	32			3.38×10^{-6}	1.33×10^{-17}	g
940828	3141	8.5	1.52×10^{-23}	21	2.3	50	2.20×10^{-6}	6.77×10^{-18}	f,i
940907	3159	7.0	6.04×10^{-23}	22	18.2	25	1.42×10^{-6}	4.18×10^{-17}	g
950531	3611	7.1	5.51×10^{-23}	23	3	80	2.44×10^{-7}	2.22×10^{-16}	j
950907	3779	7.5	3.81×10^{-23}	35	7	80	3.89×10^{-7}	9.63×10^{-17}	j
950918	3805	7.7	3.17×10^{-23}	20	40	90	8.21×10^{-7}	3.80×10^{-17}	g
950922	3814	7.0	6.04×10^{-23}	46	5	90	1.04×10^{-6}	5.71×10^{-17}	j
951117	3909	7.0	2.40×10^{-23}	18	25	90	2.86×10^{-6}	2.08×10^{-17}	g,k
		7.0	2.40×10^{-23}	25			3.15×10^{-6}	1.89×10^{-17}	g
951124	3918	7.4	4.18×10^{-23}	23.1	150	85	1.33×10^{-5}	3.09×10^{-18}	g,k
		7.4	4.18×10^{-23}	29.5			1.56×10^{-5}	2.63×10^{-18}	g
		7.4	4.18×10^{-23}	64.1			1.68×10^{-5}	2.45×10^{-18}	g
		7.4	4.18×10^{-23}	69.0			1.68×10^{-5}	2.45×10^{-18}	g
		7.4	4.18×10^{-23}	91.5			1.68×10^{-5}	2.45×10^{-18}	g
		7.4	4.18×10^{-23}	96.4			1.68×10^{-5}	2.45×10^{-18}	g
		7.4	4.18×10^{-23}	119.4			1.86×10^{-5}	2.21×10^{-18}	g
		7.4	4.18×10^{-23}	124.3			1.86×10^{-5}	2.17×10^{-18}	g
		7.4	4.18×10^{-23}	146.8			1.89×10^{-5}	2.17×10^{-18}	g
		7.4	4.18×10^{-23}	151.7			1.89×10^{-5}	2.22×10^{-18}	g
951208	3936	7.0	6.04×10^{-23}	20	3.5	85	2.67×10^{-6}	2.22×10^{-17}	h,k
951220	4048	7.9	2.64×10^{-23}	14.8	17	95	1.24×10^{-5}	2.09×10^{-18}	g,k
960403	5407	7.0	6.04×10^{-23}	33	70	20	3.12×10^{-6}	1.90×10^{-17}	h

^aOptical flux ($\text{ergs-cm}^{-2}\text{-s}^{-1}\text{-Hz}^{-1}$)

^bTime in seconds between burst trigger and GROCSE observation

^cGRB duration in seconds

^dGROCSE coverage of $3\text{-}\sigma$ BATSE error box

^e20-2000 keV gamma-ray fluence (ergs-cm^{-2})

^fFluence (erg-cm^{-2}) from 3rd BATSE catalog (Meegan, 1996)

^gFluence calculated from spectral fit to HERB data

^hFluence calculated from spectral fit to SHERB data

ⁱData missing

Table 2. Calculation of Comparison Quantities for Selected Observations.

Name	BATSE Trigger	t_d^a s	$F_\gamma(100keV)^b$	Φ_γ^c	R_1 upper limit	R_2 upper limit
940623	3040	17.4	2.42×10^{-10}	9.28×10^{-8}	4.50×10^4	2.91×10^{-1}
		20.3	1.77×10^{-10}	6.26×10^{-8}	6.15×10^4	4.32×10^{-1}
951117	3909	18	1.72×10^{-10}	7.55×10^{-8}	8.34×10^4	4.72×10^{-1}
951124	3918	23.1	8.89×10^{-10}	5.94×10^{-7}	1.12×10^4	4.15×10^{-2}
		29.5	4.46×10^{-10}	1.64×10^{-7}	2.23×10^4	1.50×10^{-1}
		119.4	1.45×10^{-10}	1.03×10^{-7}	6.85×10^4	2.39×10^{-1}
		124.3	9.66×10^{-12}	4.65×10^{-9}	1.03×10^6	5.30
951220	4048	14.8	4.12×10^{-10}	2.66×10^{-7}	1.52×10^4	5.84×10^{-2}

^aTime in seconds between burst trigger and GROCSE observation

^bGamma-ray flux at 100 keV ($\text{ergs-cm}^{-2}\text{-s}^{-1}\text{-keV}^{-1}$)

^cGamma-ray fluence ($\text{erg-cm}^{-2}\text{-s}^{-1}$)

REFERENCES

- Allen, C. W. 1976, *Astrophysical Quantities*, (London: Athlone), 126
- Band, D. L., & Hartmann, D. 1992, *ApJ*, 386, 299
- Band, D. L. et al. 1993, *ApJ*, 413, 281
- Barthelmy, S. D. et al. 1994, in "Gamma-Ray Bursts", *AIP Conference Proceedings*, 307, ed. G. J. Fishman, J. J. Brainerd & K. Hurley (AIP: New York), 643
- Bisnovatyi-Kogan, G. S., & Illarionov, A. F. 1986 *Sov. Astr.*, 30, 582
- Chevalier, R. A. 1986, *ApJ*, 308, 225
- Cominsky, L. R., London, R. A., & Klein, R. I. 1987, *ApJ*, 315, 162
- Dermer, C. 1990, *ApJ*, 360, 197
- Epstein, R. I. 1985, *ApJ*, 291, 822
- Ford, L., & Band, D. L. 1996, *ApJ*, 473, 1013
- Greiner, J. 1992, *A&A*, 264, 121
- Greiner, J., et al. 1994, "Gamma-Ray Bursts", *AIP Conference Proceedings*, 307, ed. G. J. Fishman, J. J. Brainerd & K. Hurley (AIP: New York), 408
- Greiner, J. 1995, in *Proc. of the 17th Texas Symp., Annals of the New York Academy of Sciences*, 759, 428
- Hameury, J. M., & Lasota, J. P. 1989, *A&A*, 211, L15
- Hartmann, D., Woosley, S. E. & Arons, J. 1988, *ApJ*, 332, 777
- Ho, C., & Epstein, R. I. 1989, *ApJ*, 343, 277

- Hudec R. 1993, A&AS, 97, 49
- Hudec, R. 1995a, A&SS, 231, 239
- Hudec, R. et al. 1995b, A&SS, 231, 311
- Hurley, K. et al. 1994, Nature, 372, 652
- Hurley K. et al. 1997, "Gamma-Ray Bursts", AIP Conference Proceedings, 384, ed. C. Kouveliotou, M. F. Briggs, G. J. Fishman (AIP: New York), 422
- Jennings, M. C., 1983, ApJ, 273, 309
- Katz, J. I. 1985, ApL, 24, 183
- Katz, J. I., & Jackson, S. 1988, A&A, 197, 29
- Katz, J. I. 1994, ApJ, 432, 107
- Kholopov, P. N. 1987, "General Catalog of Variable Stars", 4th Edition, (Moscow, Nauka), Vol. III
- Lee, B., et al. 1997, "Gamma-Ray Bursts", AIP Conference Proceedings, 384, ed. C. Kouveliotou, M. F. Briggs, G. J. Fishman (AIP: New York), 671
- Liang, E. P. 1985, Nature, 313, 202
- London, R. A., & Cominsky, L. R. 1983, ApJL, 275, L59
- McNamara, B. J. et al. 1995, A&SS, 231, 251
- McNamara, B. J. et al. 1996, Proc. ApJS, 103, 173
- Meegan, C.A., et al. 1996, ApJS, 106
- Melia, F. 1988, ApJL, 324, L21

- Melia, F., Rappaport, S. A., & Joss, P. C. 1986, *ApJL*, 305, L51
- Meszaros, P., & Rees, M. 1993, *ApJ*, 405, 278
- Meszaros, P., Rees, M., & Papathanssiou, H. 1994, *ApJ*, 432, 181
- Meszaros, P., & Rees, M. 1997, *ApJ*, in press
- Paczynski, B., & Xu, G. 1994, *ApJ*, 427, 708
- Papathanssiou, H., & Meszaros, P. 1996, *ApJ*, 471, L91
- Park, H. S. et al. 1990, *SPIE* 1306, "Aquisition, Tracking, and Pointing IV", 293
- Park, H. S. et al. 1997 "Gamma-Ray Bursts", *AIP Conference Proceedings*, 384, ed. C. Kouveliotou, M. F. Briggs, G. J. Fishman (AIP: New York), 408
- Rappaport, S. A., & Joss, P. C. 1985, *Nature*, 314, 242
- Rees, M., & Meszaros, P. 1992, *MNRAS*, 258, 41P
- Rees, M., & Meszaros, P. 1994, *ApJ*, 430, L93
- Ricker, G. et al. 1988, in *Nuclear Spectroscopy of Astrophysical Sources*, ed. N. Gehrels and G. H. Share, (AIP: New York), 407
- Ruderman, M. 1987, in *Proc. 13th Texas Conf. on Relativistic Astrophysics*, ed. M. P. Ulmer (Singapore: World Scientific), 448
- Sari, R., Narayan, R., & Piran, T. 1996, *ApJ*, 473, 204
- Schaefer, B. 1981, *Nature*, 294, 722
- Schaefer, B. 1984, *ApJ*, 286, L1
- Schaefer, B. 1987, *ApJ*, 323, L47

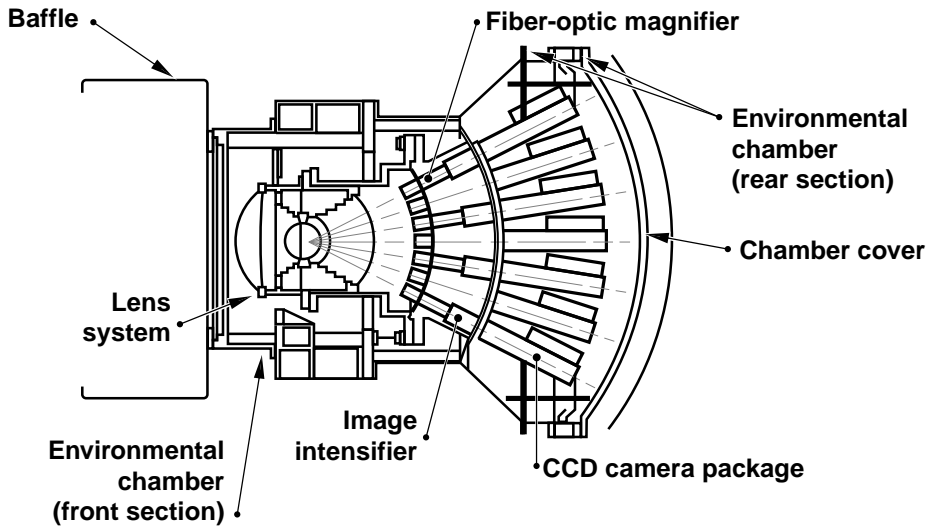
Schaefer, B. 1994, "Gamma-Ray Bursts", AIP Conference Proceedings, 307, ed. G. J. Fishman, J. J. Brainerd & K. Hurley (AIP: New York), 382

Sturrock, P. 1986, Nature, 321, 47

Tavani, M. 1996a, PRL, 76, 3478

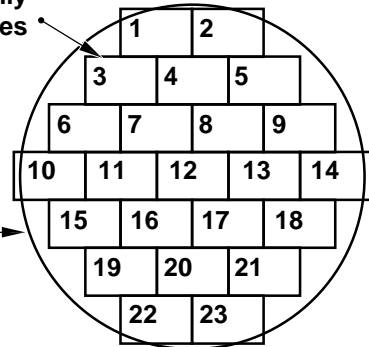
Tavani, M. 1996b, ApJ, 466, 768

Vanderspek, R., Krimm, H. A., & Ricker, G. R. 1994, "Gamma-Ray Bursts", AIP Conference Proceedings, 307, ed. G. J. Fishman, J. J. Brainerd & K. Hurley (AIP: New York), 438



Rear view of the image areas of 23 fiber-optically coupled intensified camera modules

Imaging area of 60° field-of-view,
f/2.8, 89 mm aperture lens,
250 mm focal length,
250 mm diameter focal surface



Demagnification: 3.8:1
image to CCD reduction



GROCSE Imaging System

Fig. 1.— The GROCSE system showing the fish-eye lens with fiber optic couplers mounted on the curved focal surface. Each fiber optic bundle for each camera is cemented to an intensifier and then imaged onto a CCD. The lay out of the 23 cameras viewing 60° field is depicted in the second panel. The entire instrument is mounted on a heavy-duty rapidly

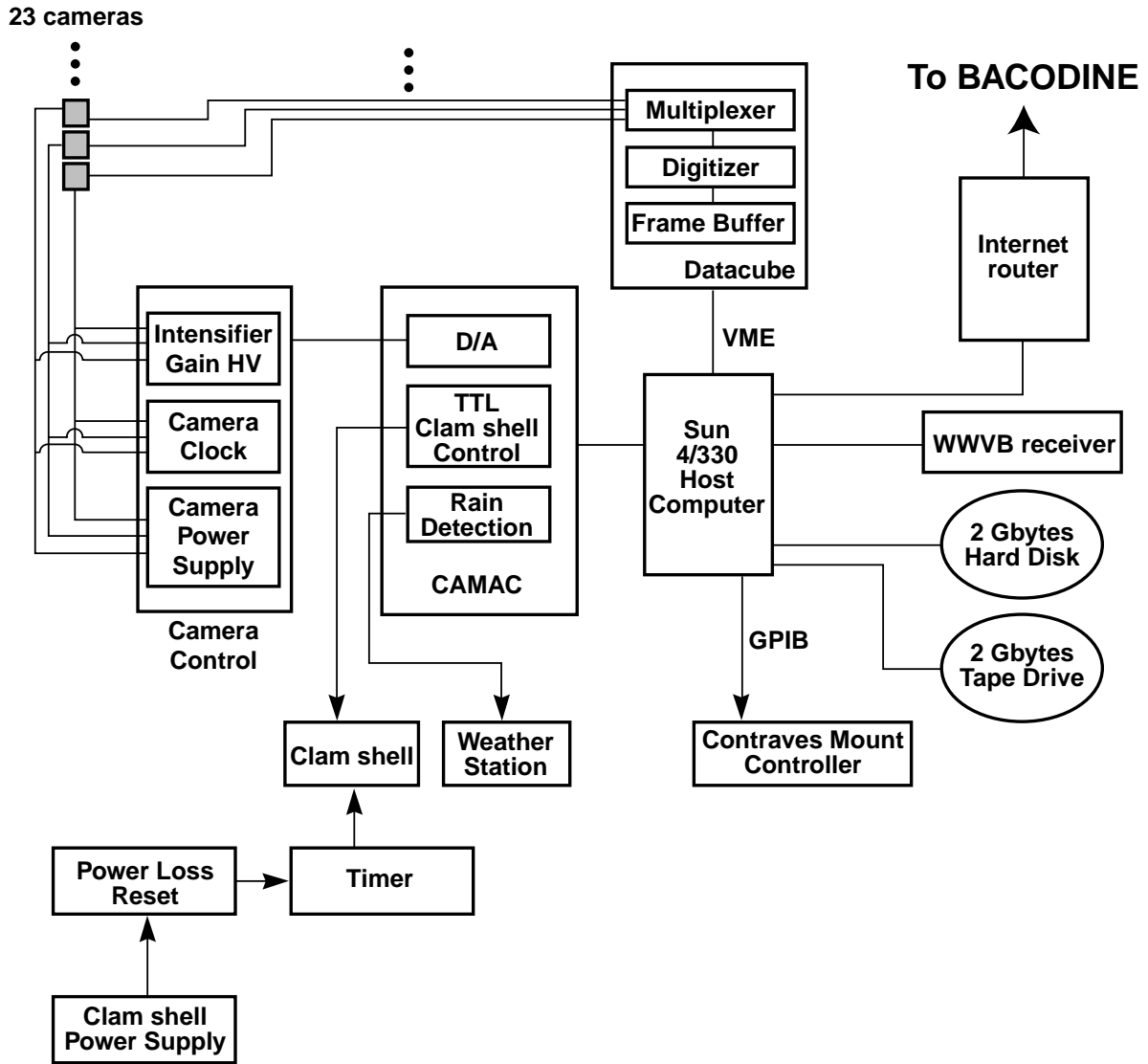


Fig. 2.— Schematic drawing of the GROCSE data acquisition system.

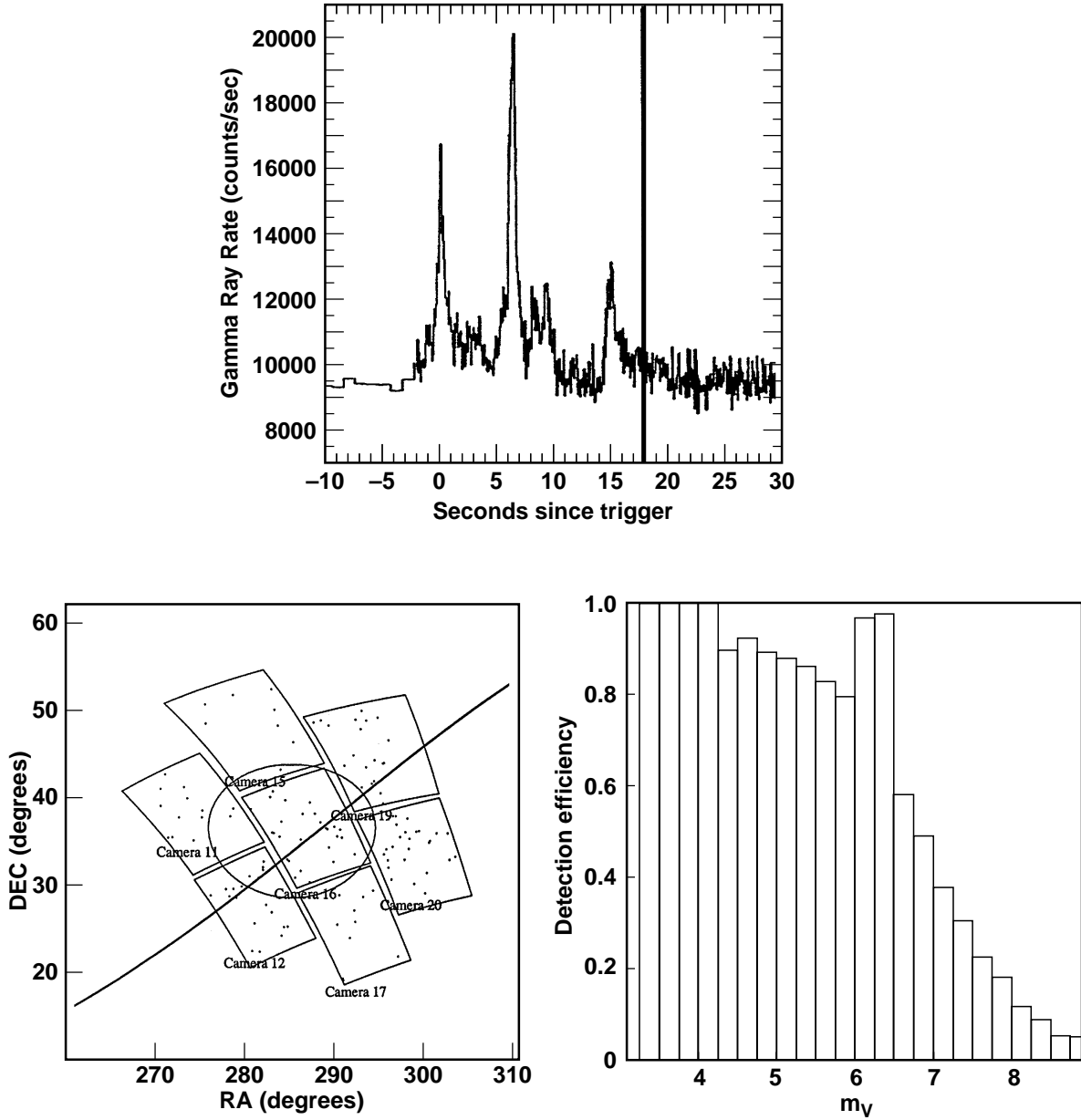


Fig. 3.— GRB 951117 (BATSE Trigger 3909) event. The first panel is the BATSE light curve. The BATSE trigger occurred at time zero. Shown on the ordinate is the count rate in counts/s. The vertical line represents the instant when GROCSE imaging began. The second panel is the GROCSE coverage of this event. The $3\text{-}\sigma$ BATSE error circle and the IPN annulus are superimposed on the GROCSE rectangular field. All GROCSE image exposure times were 0.50 s. The third panel shows the star count versus magnitude. Note that the completeness magnitude is defined as the level for which all stars are observed while the limiting magnitude is the brightness where only half the stars are observed.

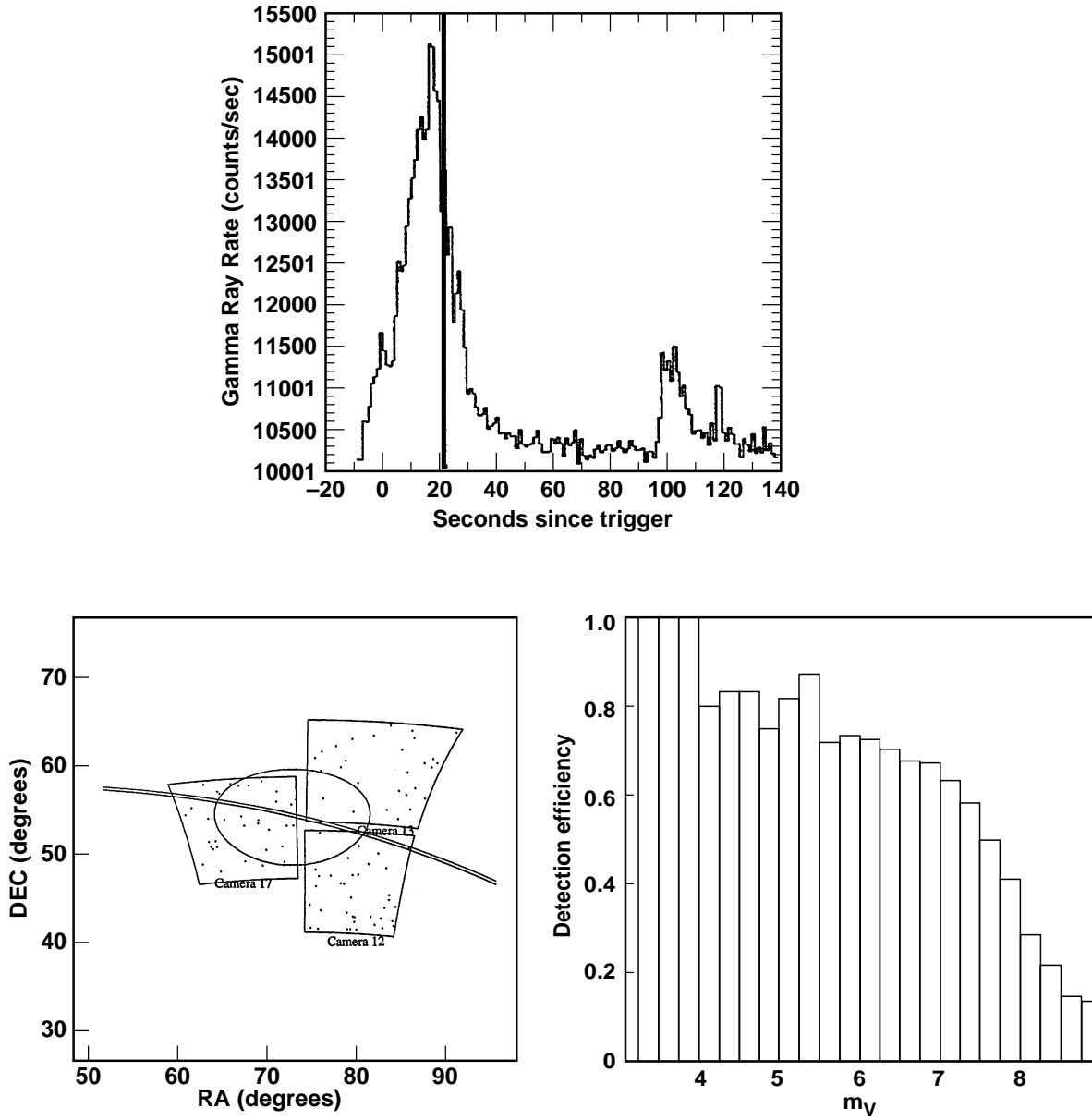


Fig. 4.— GRB 951124 (BATSE Trigger 3918) event.

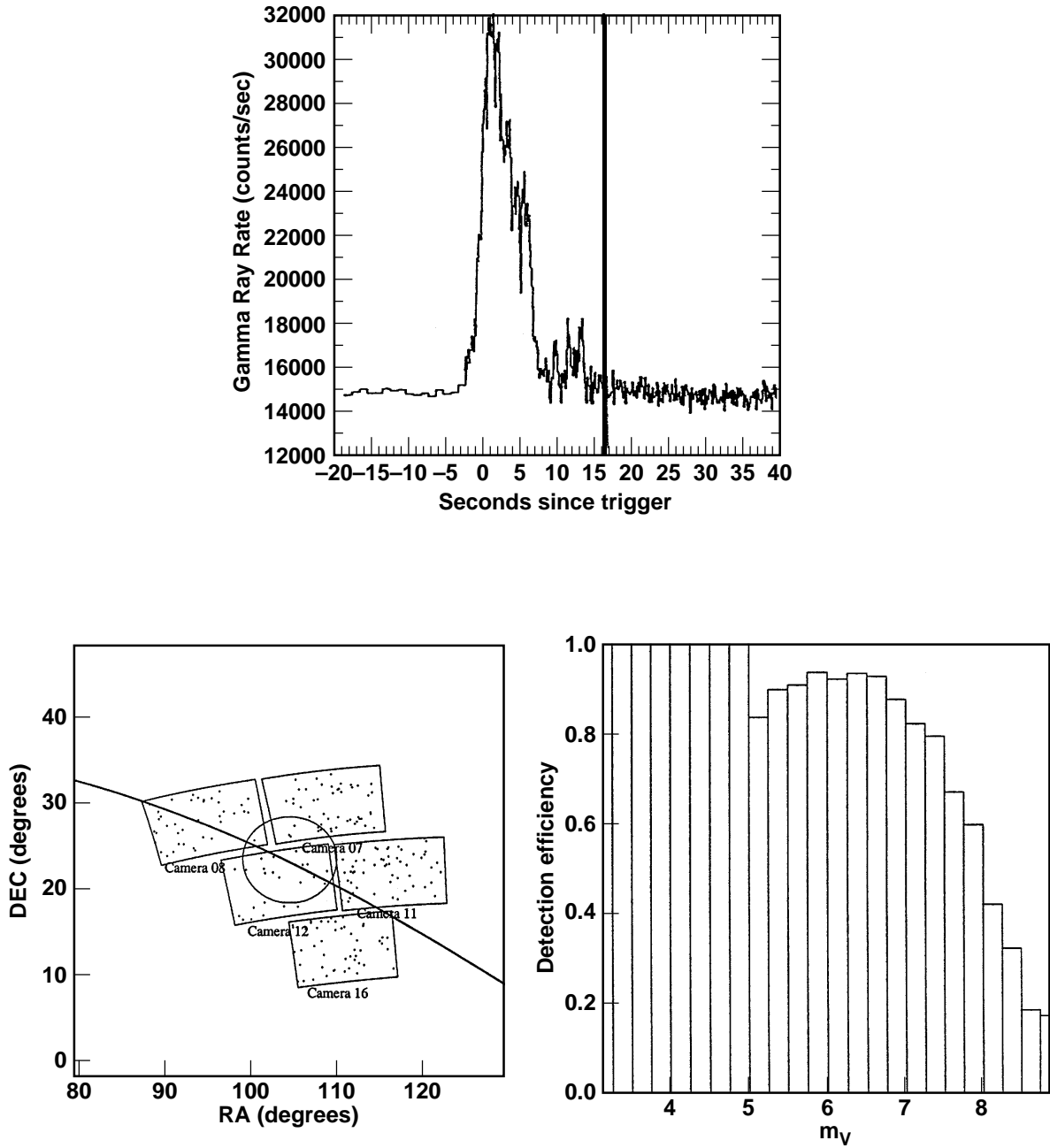


Fig. 5.— GRB 951220 (BATSE Trigger 4048) event.